Experimental test on an RC beam equipped with embedded barometric pressure sensors for strains measurement

Original
Experimental test on an RC beam equipped with embedded barometric pressure sensors for strains measurement / Tondolo, F.; Matta, E.; Quattrone, A.; Sabia, D.. - In: SMART MATERIALS AND STRUCTURES. - ISSN 0964-1726. - 28:5(2019), p. 055040. [10.1088/1361-665X/ab1172]

Publisher:
Institute of Physics Publishing

Published
DOI:10.1088/1361-665X/ab1172

Experimental test on an RC beam equipped with embedded barometric pressure sensors for strains measurement

F. Tondolo [1], E. Matta [2], A. Quattrone [1], D. Sabia [1].
[1] *Dept. Structural, Geotechnical and Building Eng., Politecnico di Torino – Italy,*
Email: francesco.tondolo@polito.it; antonino.quattrone@polito.it; donato.sabia@polito.it
[2] *Dept. Architecture and Design, Politecnico di Torino – Italy, Email:* emiliano.matta@polito.it

Abstract

The current trend in structural health monitoring (SHM) is to install increasingly large numbers of distributed, heterogeneous types of sensors, for a timely and exhaustive detection of any possible damage scenario evolving in the system. These sensors should be low-cost, easy to install, robust and durable. Among others, strain remains one of the most straightforward measurands for monitoring the state of a structural element and for assessing its health condition. However, for application to reinforced concrete structures, currently available strain sensing devices, such as electric strain gauges or fibre optic sensors, do not fully satisfy the aforementioned requirements, generally proving difficult to install, fragile and expensive. In this paper, an innovative monitoring technology, called Smart Steel System (S3), is proposed that measures strains in reinforced concrete members, by incorporating commercial barometric pressure MEMS sensors in appropriate sealed cavities embedded in the reinforcing steel bars. The results of an experimental campaign are reported, in which a reinforced concrete beam, instrumented with both S3 devices and conventional electrical strain gauges, is subjected to increasing loading and unloading cycles until collapse. The tests show the superior robustness of the S3 system during construction and loading as well as its good sensing accuracy, demonstrating its potential for a massive use in SHM applications.

Keywords: structural health monitoring, reinforced concrete, strain measuring system, low-cost technology, embedded device, barometric sensor, MEMS, electric strain gauge.

1. Introduction

Structural health monitoring (SHM) is increasingly applied worldwide both on new structures, to verify or correct the design assumptions (“design by monitoring”) and to supervise the construction process (enhancing its safety and speed), and on existing structures, to allow for a continuous assessment of their quality and reliability, especially when replacement of obsolete structures in highly urbanized contexts is required. Lynch and Loh (2006) discuss the advancement in sensor technologies, the spread of smart materials and structures and the development of wireless communication platforms as the key opportunities for SHM growth, predicting a future where every structure will be permanently, pervasively and (nearly-) automatically monitored since its construction [1]. Appropriate SHM strategies can provide for a continuous condition assessment of civil engineering assets, increasing their quality and safety levels and reducing their maintenance costs [2-5]. Despite its great potential, SHM is still not applied at a large scale and in a systematic manner to civil structures, even when its benefits would be substantial. This is mainly due to the complexity and cost of monitoring large infrastructures, which implies installing and interrogating large numbers of sensors, ensuring their effectiveness through the years, and managing and interpreting huge amounts of data. All these factors have so far confined SHM to be mainly used as a research tool [6].

While data management and interpretation is progressively being solved through big-data approaches, the high cost of the measuring system (including sensors, connections and acquisition units) remains one of the most critical points, and asks for a new paradigm in sensing technology. Currently, various sensor types exist for civil SHM purposes, such as electric strain gauges [8], accelerometers [10, 11], inclinometers, GNSS-based sensors, acoustic emissions [12], wave propagation devices [7] and several fibre optic sensors (FOS) of either distributed or local type [8, 9]. Each of them presents a preferable application field, as well as genuine challenges when deployed in the real world. Recently, a growing use is reported of low-cost MEMS sensors, initially developed for the consumer markets and subsequently used for SHM purposes, including accelerometers, inclinometers, temperature and humidity sensing devices [13-15]. Promising advancements in strain sensing technology are also currently ongoing in other research fields, whence significant contaminations are expected in the near future [16-19].

One of the most straightforward ways to assess the condition state of a structural element is the analysis of the deformations in different points along its length. In reinforced concrete (RC) structures, strain monitoring can be performed by focusing either on the concrete matrix or on the steel bars. Strains measured in the concrete matrix are affected by the wide micro variability of concrete mechanical properties, inherent in its nature of composite material. In this case, the sensing device must have dimensions comparable with the maximum aggregate size, for example by recurring to macro-skeletons, flanges or jackets. These large dimensions reduce the advantages of using modern miniaturized technologies and cause a disturbance of the local stress field. Moreover, strain measurements in the concrete matrix are highly affected by the opening of cracks. Alternatively, skin sensor arrays such as the soft elastomeric capacitor (SEC) have been recently proposed for the monitoring of RC structures [20], acting as surface strain gauges transducing local strains into changes in capacitance. Other solutions come from non-contact monitoring systems, capable to reconstruct cracking and deformation conditions both on the external surface and in the inner volume of the structure. Digital Volume Correlation or 3D Digital Image Correlation [21, 22] allow to measure a full strain tensor deep inside a body without disturbing the strain field by the presence of a measuring device. However, they both require the presence of physical inclusions to create a 3D speckle and a complete 3D vision.

Conversely, strain measurements in steel reinforcing bars take advantage of the uniform material characteristics both in tension and compression, resulting in less scattered results and in an easier interpretation of the structural response. In existing applications of instrumented bars, local strain transducers, such as electrical systems and fiber optic systems (FOS), are usually glued on the surface or incorporated in longitudinal grooves machined along the bar [23]. Distributed measurements of strain can be obtained by distributed FOS, which can measure the strain along the whole length of the glued fiber [24]. However, in FOS applications the cost of the interrogating unit is often so high that only a single unit can be afforded on a given structure, or even on different structures, thus imposing severe limitations to the monitoring layout (e.g. a reduction in the number of the available channels), which generally discourage the use of FOS in continuous monitoring applications. Furthermore, both electrical and FOS strain transducers need to be installed by specialized personnel and may be damaged during all phases of installations (from gluing to concrete casting).

Alternatively, embedding sensors can dramatically reduce the risk of damaging them during installation, and can also avoid the local perturbations which a glued sensor might produce at the interface between concrete and steel. This solution was adopted by Mains in his experimental work on bond tests [25], where the reinforcing bars were cut longitudinally in two halves and strain gauges were embedded in between, before welding them again to reconstruct the original bar. This procedure proved particularly effective and has been recently used again in Lagier et al. [26].

Embedding the strain transducer in the reinforcing bar is also at the core of the new called Smart Steel System (S3) technology proposed by Tondolo [27]. The S3 system consists of an instrumented reinforcement steel bar, which can achieve strain-sensing capabilities through embedding an ordinary, low-cost, Micro Electro-Mechanical Systems (MEMS) ultra-compact piezoresistive barometric sensor, measuring pressure and temperature. According to this concept, a sealed cavity is made in the bar, filled with air and hosting the MEMS sensor; the temperature and pressure readings collected by the MEMS sensor are used to evaluate the cavity volume variations, and then correlated with the bar axial deformation. S3 presents significant advantages over current strain-measurement devices, proving cheap, durable, easy to install, robust to mechanical shocks and chemical aggression. The theoretical framework of S3 is already explained in [28], and there validated through a preliminary test campaign on a bare bar subjected to a variety of axial load tests, including monotonic tests until rupture and repeated load cycles of variable frequency and amplitude. That study allowed to conclude that, as long as the S3 sensing units are embedded in a single, isolated bar, their sensibility and repeatability are acceptable for ordinary monitoring applications, even under repeated load cycles, up to certain cyclic frequencies. In this paper, the first application of S3 to a real structural element is reported, consisting of a reinforced concrete beam subjected to a classical four-point bending test, under loading and unloading cycles of increasing amplitude, until collapse. A comparison between S3 and standard electrical strain gauges is also reported and commented. Of course, the quasi-static load cycles applied in this study do not cover all situations possibly encountered by generic reinforced concrete structures during their lifetime, and particularly not dynamic or fatigue loading conditions. Therefore, referring to [28] for a closer look into the dynamic and cyclic response of a single S3-instrumented bar, this paper rather focuses on testing the S3 system within a real reinforced concrete structure, that is monitored while spanning all possible statically damaged states, from its original intact condition until collapse. In this context, for the first time an S3-smart bar is indeed observed in material and structural connection with its surrounding concrete matrix.

2 Smart steel system under testing

2.1 Basic principles of the tested S3 system

In its basic configuration, S3 consists of a steel bar hosting one or more sensing units. Each unit is realized as a hermetic cavity drilled within the bar and equipped with a low-cost MEMS sensor, which measures pressure and temperature of the fluid (typically air) contained in the cavity [27]. If the bar is subjected to axial deformations locally around a cavity, the volume of that cavity varies according to the laws of continuum mechanics. The extent of the volume variation can be computed by combining pressure and temperature data from the embedded sensor, and can be finally used as a measure of the local axial strain. Once incorporated in a reinforced concrete structure, the resulting instrumented smart steel bar will integrate both structural and sensing functions. These latter functions, apart from the required connections for data transmission and power supply, will be safely performed in the protected and virtually aseptic environment of the sealed cavity.

Assuming that the fluid in the cavity is air and can be approximated as an ideal gas, and denoting by $p = p(t)$, $T = T(t)$ and $V = V(t)$ respectively the pressure, temperature and the volume of the fluid in the cavity at time t, and finally by Δp, ΔT and ΔV their variations with respect to their initial values V_0, p_0 and T_0 at time $t = 0$, the volume deformation $\Delta V/V_0$ can be derived, at any t, from the monitored time histories of p and T, through the following relation [28]:

$$\frac{\Delta V}{V_0} = \left(1 + \frac{\Delta T}{T_0}\right) \Big/ \left(1 + \frac{\Delta p}{p_0}\right) - 1 \qquad (1)$$

In Eq. (1), the volume deformation $\Delta V/V_0$ of the cavity reflects any local axial deformation of the bar, essentially caused by either mechanical or thermal actions. Assuming for simplicity a linear superposition of mechanical and thermal effects, it can be written:

$$\frac{\Delta V}{V_0} = \left(\frac{\Delta V}{V_0}\right)_M + \left(\frac{\Delta V}{V_0}\right)_T \tag{2}$$

where $(\Delta V/V_0)_M$ and $(\Delta V/V_0)_T$ represent the volume deformations of the cavity related to, respectively, the mechanical and thermal deformations experienced by the steel bar locally around the cavity. To obtain the term $(\Delta V/V_0)_M$, which provides the desired measure of local axial stresses or strains in the bar, a two-step calibration process is required, including first a thermal calibration and then a mechanical calibration.

The thermal calibration provides the term $(\Delta V/V_0)_T$ in Eq. (2) by experimentally establishing its relation with the temperature variations experienced by the bar locally around the cavity, assuming for simplicity that these variations correspond to the temperature variations ΔT measured in the cavity. Such relation can be experimentally obtained by monitoring the response of S3 when the steel bar is subjected to temperature variations in unloaded conditions. In this circumstance, $(\Delta V/V_0)_M$ is null and Eq. (2) provides the experimental relation $f(\cdot)$ existing between $(\Delta V/V_0)_T$ and ΔT as follows:

$$\left(\frac{\Delta V}{V_0}\right)_T = \left.\frac{\Delta V}{V_0}\right|_{unloaded} = f(\Delta T) \tag{3}$$

where $\Delta V/V_0|_{unloaded}$ is the volume deformation of the cavity computed according to Eq. (1) in dependence on the pressure and temperature variations Δp and ΔT. This thermal calibration test can be conducted in a temperature controlled chamber [28] or even in ambient temperature conditions provided that appropriate temperature variations are explored. Once the thermal calibration is available, Eqs. (1) to (3) provide $(\Delta V/V_0)_M$, in any temperature conditions, as a function of Δp and ΔT.

The subsequent mechanical calibration test, conducted by imparting the steel bar a controlled axial force $F(t)$ in uncontrolled temperature conditions, establishes the experimental relation $g(\cdot)$ existing between $(\Delta V/V_0)_M$ and some significant measurable quantity representative of the mechanical response of the bar locally around the cavity. As far as the bar response is in its linear elastic domain, various alternative stress and strain quantities can be chosen [28]. Beyond the linear elastic domain, instead, strain quantities are much more strongly correlated with $(\Delta V/V_0)_M$. In this paper, two alternative mechanical quantities are chosen for correlation with $(\Delta V/V_0)_M$, namely the axial force F itself and the corresponding equivalent axial strain on the steel bar gross area A, defined as:

$$\varepsilon = \frac{F}{EA} \tag{4}$$

where E is the steel Young modulus. Because the mechanical calibration tests are performed in the linear elastic range of the bar response, the following proportional relations can be experimentally identified between $(\Delta V/V_0)_M$ and the two said mechanical quantities:

$$\left(\frac{\Delta V}{V_0}\right)_M = g_1(F) = \frac{F}{k_1} \tag{5}$$

$$\left(\frac{\Delta V}{V_0}\right)_M = g_2(\varepsilon) = \frac{\varepsilon}{k_2} \tag{6}$$

where k_1 and $k_2 = k_1/EA$ are the mechanical calibration coefficients transforming the measured volume variation (obtained from Eq. (1) and thermally corrected by Eqs. (2) and (3)) into, respectively, the estimated axial force F and the estimated equivalent axial strain ε experienced by the bar locally around the cavity. Complemented with Eqs. (1) to (3), Eqs. (5) and (6) are therefore the fundamental relations to interpret the pressure and temperature data coming from the sensor. They both rigorously hold as long as the steel bar is stressed in its the linear range. Outside it, Eq. (5) is no longer applicable for the estimation of F [28], while Eq. (6), as it will be shown later, still provides a reasonable estimation ε of the axial strain around the cavity.

2.2 Technical details of the tested S3 system

Although generally applicable to other types of structural elements, the S3 system considered in this paper is incorporated into ribbed steel bars for the reinforcement of concrete structural elements. One or more sensing units are realized in each instrumented bar. The instrumented bars have 20 mm diameter, and each sensing unit is hosted in a cavity, in the shape of a transversal cylindrical drilled hole having diameter 4 mm and depth 18 mm. Each cavity is filled with air and hosts a hard printed circuit board (PCB). On the hard PCB a typical commercial MEMS barometric ultra-compact piezoresistive sensor is mounted, commonly used in smartphones and available on the market at a cost of about 2$. The MEMS sensor has dimensions approximately 2x3x1 mm, and measures pressures in the range from 260 hPa to 1260 hPa and temperatures in the range from -30 °C to 105 °C. An electrical feedthrough at the entry of each cavity seals the cavity and connects the hard PCB inside with a soft PCB outside. The soft PCB, lodged into a groove machined along the bar, communicates with the acquisition system, which acts as a connecting wire receiving power and transmitting data. The cavity and the groove determine a maximum 24% reduction of the bar transversal section, and therefore a considerable reduction of the overall bar resistance and ductility, as shown in [28].

2.3 Preliminary calibration of the S3 system

A total of four sensing units are used in the presented experimental campaign. Units S3-1 and S3-3 are embedded in steel bar #1, while units S3-3 and S3-4 are embedded in steel bar #2. Before starting the experimental campaign, preliminary thermal and mechanical calibration tests are conducted on each sensing unit, in order to experimentally determine the relations expressed by Eqs. (3), (5) and (6).

The thermal calibration is conducted by letting the two instrumented bars undergo uncontrolled ambient temperature fluctuations for several hours, at zero axial load. During this test, pressure and temperature variations are continually monitored by the barometric sensor, so that both the reconstructed $(\Delta V/V_0)_T$ and the measured ΔT are known at every time instant t. This allows for the identification of the experimental relation $f(\cdot)$ in Eq. (3), which in this study, in view of the relatively limited environmental temperature variations occurred during ambient tests, is assumed to be expressed by a linear polynomial, instead of the cubic one adopted in [28].

The mechanical calibration is conducted by separately subjecting the two instrumented bars to uniaxial tensile force tests, performed in uncontrolled thermal conditions. The load is imparted through a universal testing machine, having a maximum load capacity of 250 kN. To avoid the insurgence of any plastic strain, the maximum applied load is limited to 40 kN, corresponding to about 160 MPa of tensile stress on the bar net transversal section. This maximum load is reached during a complete loading and unloading cycle consisting of 8 steps of 5 kN each.

The results of the mechanical calibration test are summarized for the sensing unit S3-1 in Figure 1, where the time histories are reported of, respectively, the applied force (1a), the measured pressure (1b) and temperature (1c) variations, the volume variations (1d) (corrected to account for the temperature variations occurring during the test), the volume-to-force calibration function (1e), and the comparison between the applied and the estimated axial force (1f).

In particular, the angular coefficient of the straight line in Figure 2e represents the mechanical calibration coefficient k_1 for this sensing unit. The corresponding mechanical calibration coefficient k_2 can be calculated dividing k_1 by the axial stiffness EA referred to the bar gross transversal area (where E = 200 GPa is assumed). From Figure 1, a satisfactory matching between the applied and the estimated load is evident (Figure 1f), reflecting the substantial proportionality and the limited hysteresis inherent in the volume-to-force relations (Figure 1e). By repeating the procedure for the other three sensing units, the calibration coefficients k_1 and k_2 are eventually obtained, which are reported for completeness in

Table 1. It can be observed that these coefficients appear quite homogeneous among the four units. It might be noted that pressure and temperature variations, respectively shown in Figures 1b and 1c, do not return to zero after complete unloading. This is due to the environmental temperature of the laboratory having changed during the 20 minutes-long mechanical calibration test, as already pointed out in previous tests on single S3-instrumented bars [28]. The modified thermodynamic conditions within the cavity would lead to erroneous estimation of the cavity volume variations, if thermal compensation were not used for correcting the $(\Delta V/V_0)_M$ term. Such correction, in fact applied in Figure 1d, indeed ensures a $(\Delta V/V_0)_M$ time history that accurately tracks the F time history, returning to zero after unloading. Thanks to this thermal compensation, the S3 system works effectively under any number of repeated cycles, as demonstrated in [28], and coefficients k_1 and k_2 do not vary with the number of cycles.

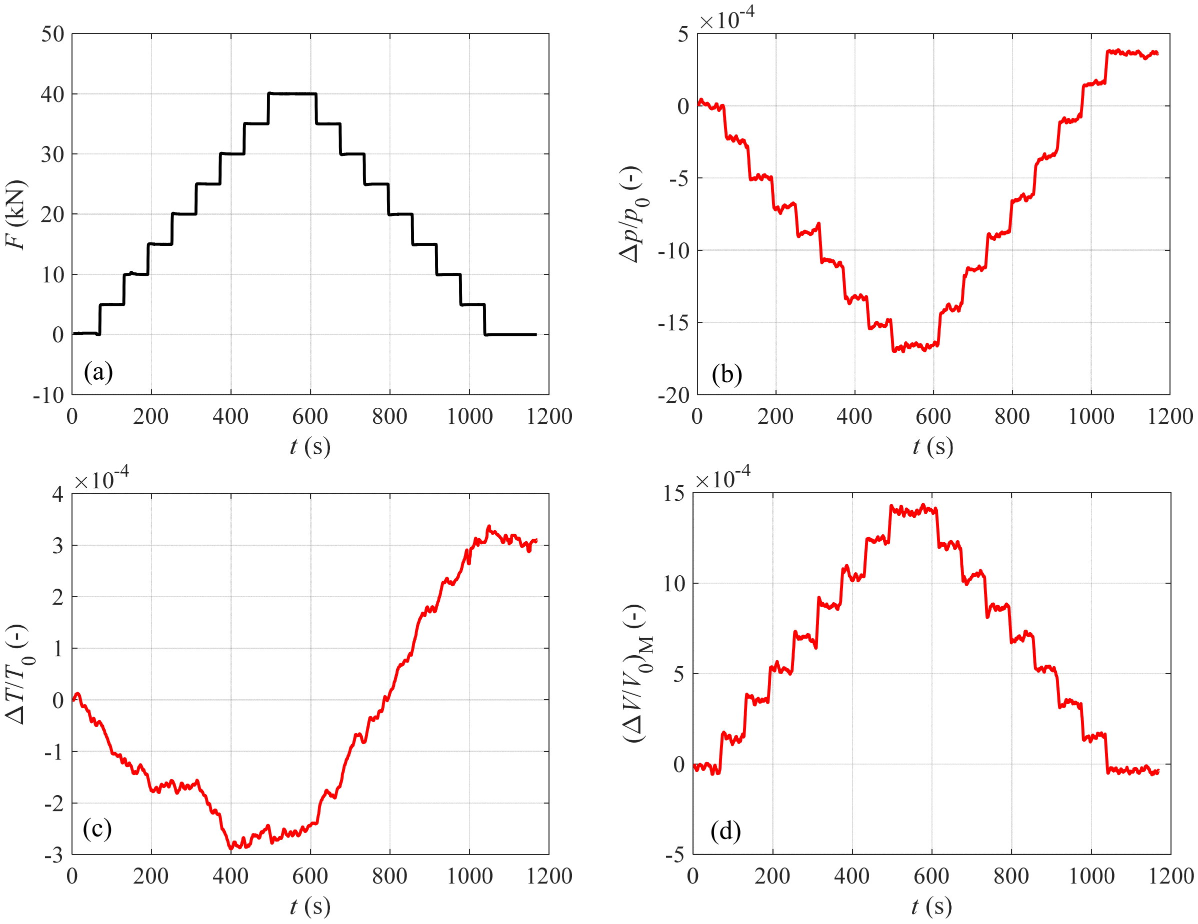

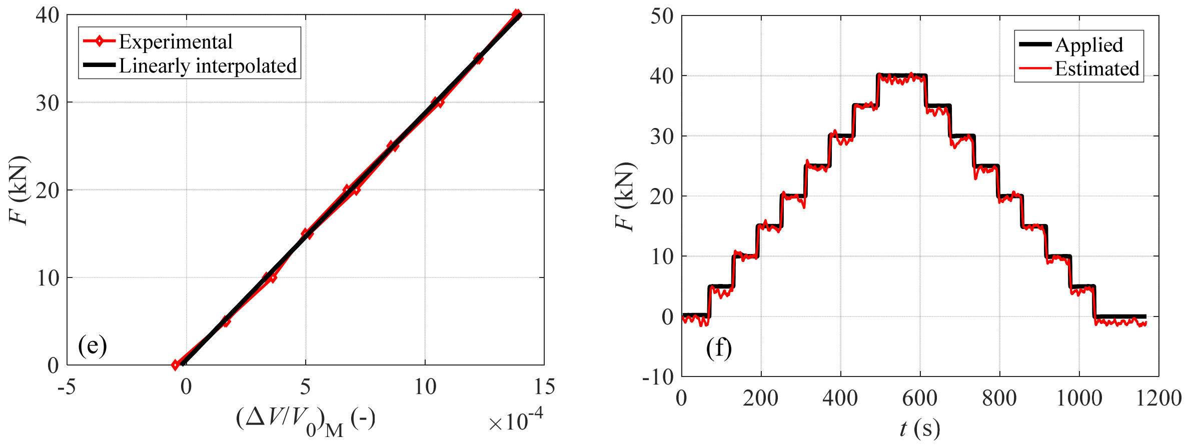

Fig. 1. Mechanical calibration test for the S3-1 unit: (a) applied force; (b) measured pressure; (c) measured temperature; (d) reconstructed force-dependent volume variation; (e) volume-to-force calibration; (f) applied vs estimated force.

Table 1. Calibration coefficients of the four S3 sensing units.

Steel bar #	Unit	k_1 (kN)	k_2 (μm/m)
1	S3-1	$2.815\cdot10^4$	$4.481\cdot10^5$
1	S3-2	$2.646\cdot10^4$	$4.212\cdot10^5$
2	S3-3	$2.987\cdot10^4$	$4.755\cdot10^5$
2	S3-4	$2.816\cdot10^4$	$4.481\cdot10^5$

3 Experimental setup

The experimental tests focus on a reinforced concrete beam, instrumented with both S3 devices and standard linear electrical strain gauges and subjected to 11 loading and unloading cycles of increasing amplitude, up to collapse. The loading levels are established in order to gradually explore the evolution of the beam from the uncracked condition to structural failure, allowing for an exhaustive comparison of the two sensor types in all relevant scenarios.

Figure 2 respectively reports pictures of: (a) four reinforcing bars instrumented with S3 devices and electrical strain gauges (bars #1 and #2 used in the present test, bars #3 and #4 not in the scope of this paper); (b) the steel reinforcing cage of the tested beam, incorporating bars #1 and #2); (c) the beam during casting; and (d) the beam in the final test setup. The red end caps in Figure 2a protect the threaded couplers used to connect the extremities of the instrumented bars with the rest of the reinforcing cage.

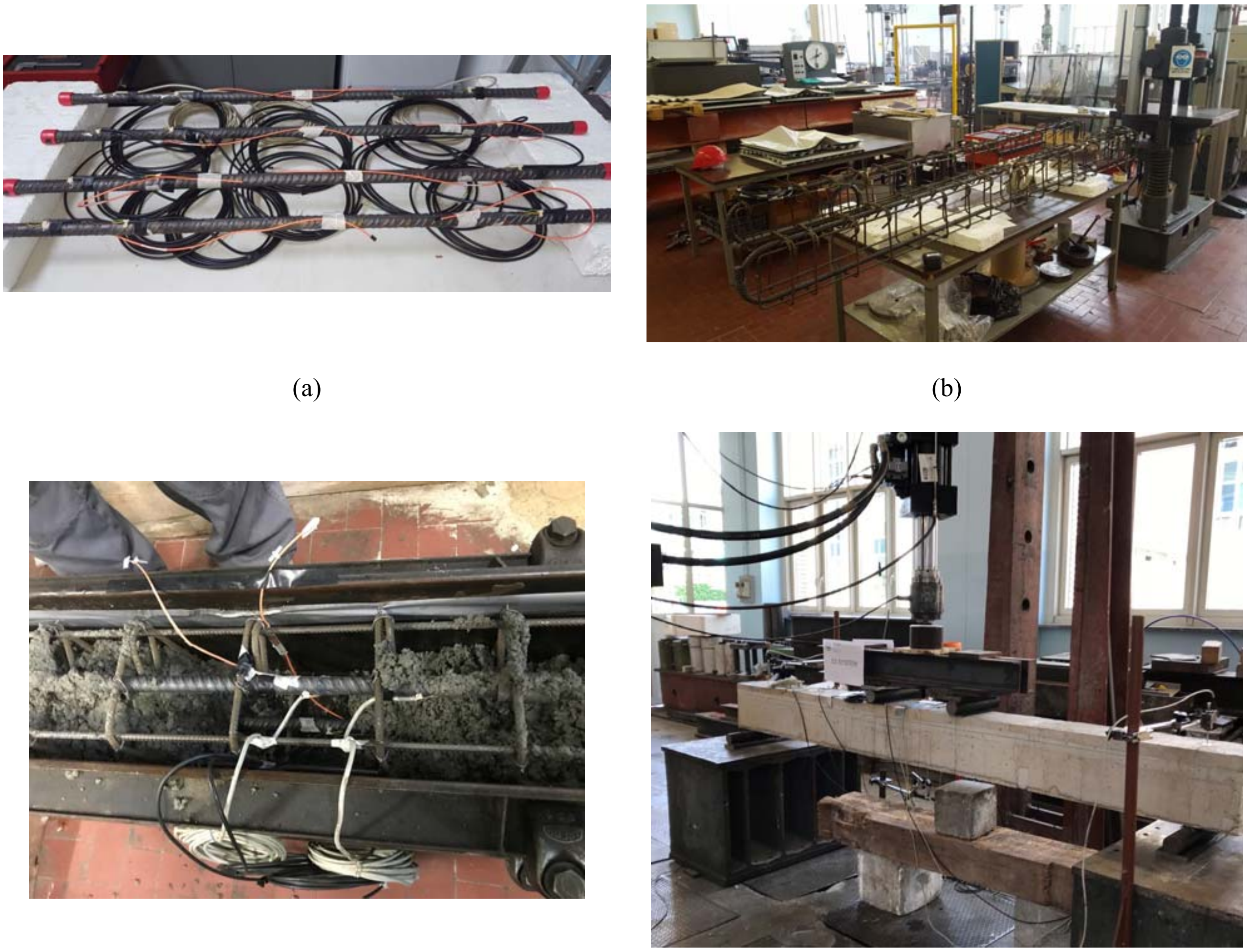

(a) (b)

(c) (d)

Fig. 2. Digital photo of the specimen under testing: (a) reinforcing bars hosting S3 units and electrical strain gauges; (b) full steel reinforcing cage; (c) casting of concrete; (d) the specimen in its final configuration under testing.

Figure 3 describes the main features of the test setup, including the load scheme, the geometry of the beam, the details of the reinforcing cage components (longitudinal bars and stirrups), and the sensors type and location.

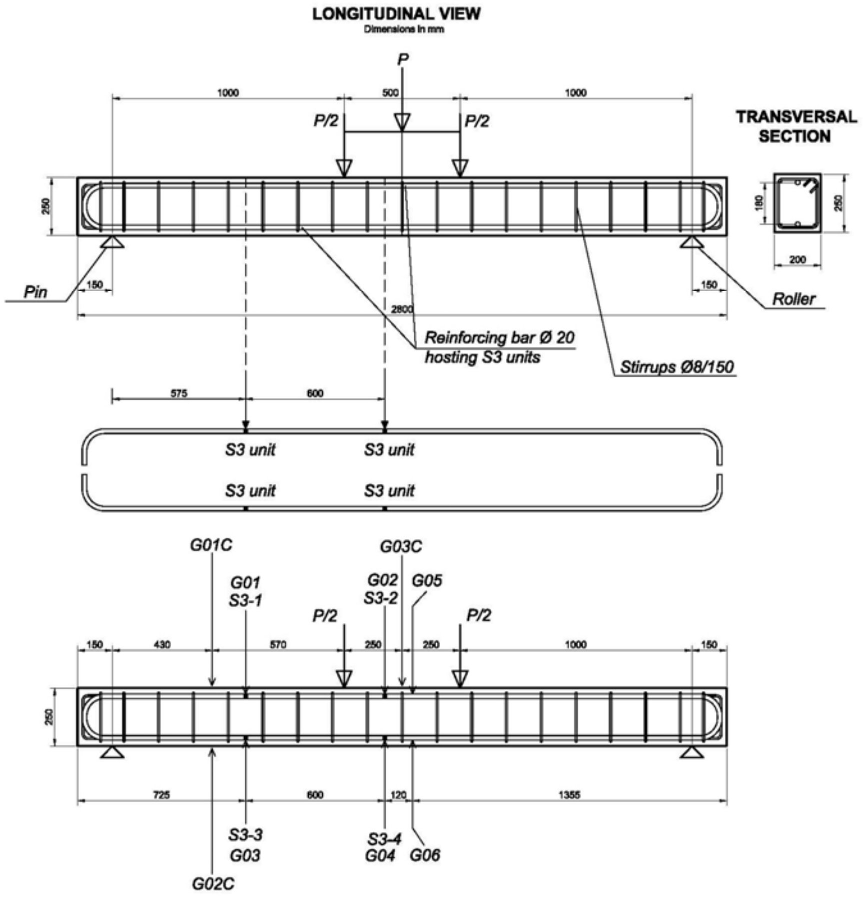

Fig. 3. Tested beam geometry and reinforcement details. Position of the sensors on the top bar (S3-1, S3-2 and G01, G02, G05), on the bottom bar (S3-3, S3-4 and G03, G04, G06), on the top beam face (G01C and G03C) and on the bottom beam face (G02C).

The load scheme reproduces a typical four-point bending test. The beam has a net length between supports of 2500 mm and transversal dimensions 200x250 mm. Its longitudinal steel reinforcement comprises, both at the top and at the bottom of the cage, two 8 mm diameter ordinary bars placed at the section corners and one 20 mm instrumented bar placed at the section midpoint (namely, bar #1 at the top and bar #2 at the bottom). Its transversal steel reinforcement comprises 8 mm diameter stirrups, placed at a constant 150 mm spacing. The concrete cover is 25 mm for the longitudinal bars. The shear span of the beam is 1000 mm; the distance between the two applied forces is 500 mm.

Of the four S3 sensing units embedded in bars #1 and #2 (see again Table 1), units S3-2 and S3-4 are located close to the beam midsection, in the zone of constant bending moment, while units S3-1 and S3-3 are located close to the shear span midsection, in the zone of linearly variable bending moment. For comparison, strain gauges G01, G02, G03 and G04 are glued on the same bars #1 and #2, at the same location of, respectively, units S3-1, S3-2, S3-3 and S3-4, but on the opposite side of the bars with respect to the S3 entries. Strain gauges G05 and G06 are also glued on, respectively, bars #1 and #2, again close to the beam midsection but at a distance from the S3 units, where the influence of the corresponding steel section reduction is deemed negligible. Finally, strain gauges G01C, G02C and G03C are directly glued on the concrete surface at the top and bottom beam faces, providing the strains at the edges of the beam section. All the electrical strain gauges are standard HBM Series Y- They are temperature-compensated with external dummy strain gauges in a full bridge configuration. Those glued on the steel bar surface have a linear measuring grid length of 6 mm and gauge factor 2.04, those glued on the beam concrete surface have a linear measuring grid length of 20 mm and gauge factor 2.11.

Figure 2c shows the orange connecting wires corresponding to S3 units S3-2 and S3-4 as well as the two grey connecting wires corresponding to strain gauges G02 and G03, exiting from the top of the beam in the constant bending moment zone. Noticeably, despite the caution used in pouring concrete, electrical strain gauges G01 and G06 broke down during casting and could not be used for testing.

Compression tests on cylindrical concrete specimens collected during casting reveal an average compressive strength of 58.3 MPa and an average tensile strength of 4.9 MPa. Reinforcing bars are made of steel B450C according to the Italian Building Code. Uniaxial tensile tests reveal for the steel bars an elastic modulus of 200 GPa, a yielding stress of 515 MPa, and an ultimate stress 620 MPa corresponding to an ultimate strain of 9%.

Figure 4 shows the converting boards attached to the edge of the beam; each board interrogates the barometric sensors and converts the digital temperature and pressure measures in analogue signals, finally collected by a multichannel data acquisition system (DAQ). The DAQ simultaneously acquires the signals coming from all the S3 systems as well as all other relevant measures: the load applied by the actuator, the actuator stroke, the signals from the electrical strain gauges and the vertical displacements of the beam in its midsection and at the supports (Figure 4).

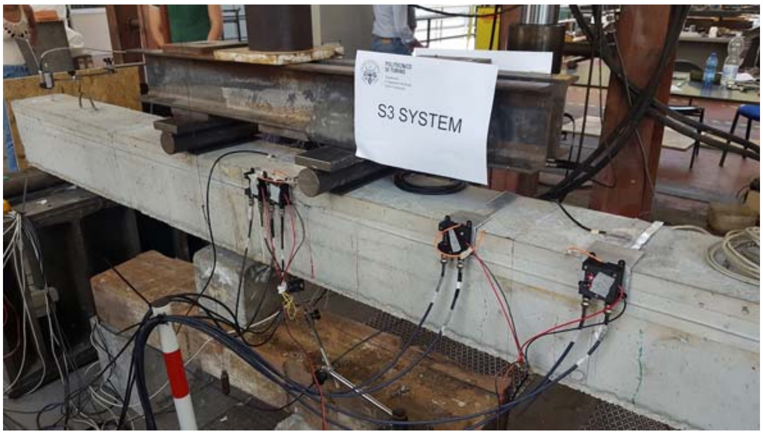

Fig. 4. Digital photo of the converter boards for the S3 units.

4 Results and discussion

A summary of the whole testing campaign is reported in Table 2. Generally denoting by P the applied load on the beam and by f the net deflection measured in the beam midsection (subtracted the average deflections at the supports), Table 2 reports, for every load cycle, the values of the load, of the deflection and of the strains measured at the time instant when the maximum load is reached in that cycle (i.e. at the end of the loading phase). The only exception is the last cycle (#11), where the time instant is conventionally taken just before the failure of G04 (at t = 425 s). Additionally, the third column reports the value of the load P normalized to the ultimate load P_u = 88.2 kN (obtained at cycle #11), and the last three columns report, for the three co-located sensors pairs, the ratio between the strains measured, respectively, by the S3 type and by the strain gauges (G) type. In the last row, S3-4 and G04 are omitted because already failed when the ultimate load is reached.

Table 2. Load, deflection and strain measurements at the end of the loading phase, for each load cycle.

Cycle (-)	P (kN)	P/P_u (-)	f (mm)	S3-1 (μm/m)	S3-2 (μm/m)	S3-3 (μm/m)	S3-4 (μm/m)	G02 (μm/m)	G03 (μm/m)	G04 (μm/m)	G05 (μm/m)	S3-2/G02 (-)	S3-3/G03 (-)	S3-4/G04 (-)
01	6.0	0.07	0.28	-14	-23	6	35	-17	37	53	-11	1.33	0.15	0.65
02	12.0	0.14	0.55	-14	-76	33	86	-88	56	107	-32	0.87	0.59	0.81
03	18.0	0.20	1.00	-36	-113	46	143	-113	88	207	4.7	1.00	0.52	0.69
04	25.0	0.28	1.81	-60	-167	77	355	-160	132	409	-15	1.04	0.58	0.87
05	25.0	0.28	1.87	-67	-156	88	334	-185	138	378	-82	0.84	0.64	0.89
06	35.0	0.40	2.95	-75	-205	216	562	-220	276	636	-97	0.93	0.79	0.88
07	45.0	0.51	3.98	-109	-223	326	871	-257	453	940	-126	0.87	0.72	0.93
08	55.0	0.62	5.17	-118	-278	478	1341	-279	613	1259	-143	1.00	0.78	1.07
09	65.0	0.74	6.62	-149	-334	687	2730	-311	836	1814	-133	1.07	0.82	1.50
10	76.7	0.87	8.31	-151	-390	1079	8044	-382	1052	3465	-160	1.02	1.03	2.32
11	88.2	1.00	16.17	-115	216	2291	-	555	1704	-	-78	0.39	1.34	-

The results of load cycles #02, #06 and #10 are respectively presented in Figures 5, 6 and 8, to exemplify the cases of low, medium and high loading levels. Each figure orderly reports: (a) the time history of the applied load; (b) the beam load-deflection curve; (c) the time history of the pressure variations measured by the S3 units; (d) the time history of the temperature variations measured by the S3 units; (e) the time history of the strain estimated from the S3 measurements; (f) the load-strain curves estimated from the S3 measurements; (g) the time history of the strain measured by the G strain gauges; (h) the load-strain curves measured by the G strain gauges. For better clarity, in all figures, deflections and strains are reset to zero at the beginning of each new cycle. Also, in all figures, the co-located pairs of S3 and G sensors (see again Figure 3) are plotted in the same colour. Only exception is represented by sensors S3-1 and G05, both plotted in red although located in different beam sections.

Observing Figures 5, 6 and 8, a satisfactory performance of the S3 units is apparent, demonstrated by the acceptable matching between the S3 estimations and the G measurements at all load levels (subfigures e and f to be compared with subfigures g and h).

At the lower load level (load cycle #02 up to P = 12 kN, Figure 5), the S3 units appear to be disturbed by noise, which makes their strain estimations less stable than the strain measurements acquired by the G sensors. However, the underlying trends appear in close agreement, especially considering that for the S3 units ε is conventionally referred to the steel bar gross section, and therefore is certainly underestimated with respect to the strain occurring at the cavity location, measured by the electrical strain gauges. Observing Figure 5 and recalling Eq. (4), the maximum strain, stress and force in the bottom bar around the beam midsection are approximately: ε = 100 μm/m; σ = 20 MPa; F= 6.3 kN. At this low load level the noise in S3 measurements is anyway not a significant drawback, because every bar is still well within its linear elastic range. Despite this low load level, both S3-4 and G04 (bottom bar around midsection) show a cyclic hysteresis in the load-strain curves (Figures 5f and 5h), probably due to cracking.

At the medium load level (load cycle #06 up to P = 35 kN, Figure 6), the effect of noise on S3 strain estimations is nearly negligible. A good matching is again observed between S3 and G results. The maximum strain, stress and force in the bottom bar around the beam midsection are approximately: ε = 620 μm/m; σ = 124 MPa; F = 39 kN. These values still correspond to a steel bar in its fully elastic range. A significant hysteresis is again observed at the location of S3-4 and G04 (bottom bar around midsection), but even larger is the hysteresis observed at the location of S3-3 and G03 (bottom bar aside), due to cracking propagation towards the supports. In fact, the effects of cracks opening around S3-3 are clearly visible in Figure 6e at approximately t = 400 s. In Figure 7 the crack pattern is reported as observed at the end of this load cycle #06.

At the higher load level (load cycle #10 up to P = 76.7 kN, Figure 8), the effects of noise on S3 strain estimations are decisively negligible. The maximum strain estimated by S3-4 is around 12700 μm/m. If the bar still were in its linear elastic range, this would correspond to σ = 2540 MPa and F = 798 kN. These disproportionately high values of stress and force indicate that the bar around the cavity has undergone large plastic deformations. This is also clearly shown in Figures 8f and 8h, where the load-strain curves of both S3-4 and G04 show a significant hysteresis. Noticeably, however, the strains estimated by S3-4 are larger than those measured by G04. This indicates that the plastic deformations occurring around the cavity have a larger influence on the cavity volume variation than on the average axial strains measured at the bar surface by the strain gauge along its length. Clearly, in the presence of so large plastic deformations, the same concept of equivalent strains around the cavity loses any practical meaning. At the location of S3-3 and G03 (bottom bar aside), the maximum strain estimated by S3-3 is around 1120 μm/m. If the bar still were in its linear elastic range, this would correspond to σ = 224 MPa and F = 70 kN. In [28], the divergence from linearity for a bar equipped with S3 units was observed to appear around 50 kN. It can be concluded that during this load cycle some plastic deformations are likely to have occurred around the S3-3 cavity as well. However, their hysteretic effect on the load-strain curves in Figures 8f and 8h is limited. The overall effect of the plastic deformations around the S3-4 cavity on the beam load-deflection curve (Figure 8b) is not very significant, because of their local character. The local weakness of the instrumented steel bar evidently results in a scarce ductility of the bar itself and finally of the beam. In order to restore the original bar ductility despite the presence of the cavity hosting the S3 unit, an additional external rib should be implemented in the rolling phase as suggested in reference [27].

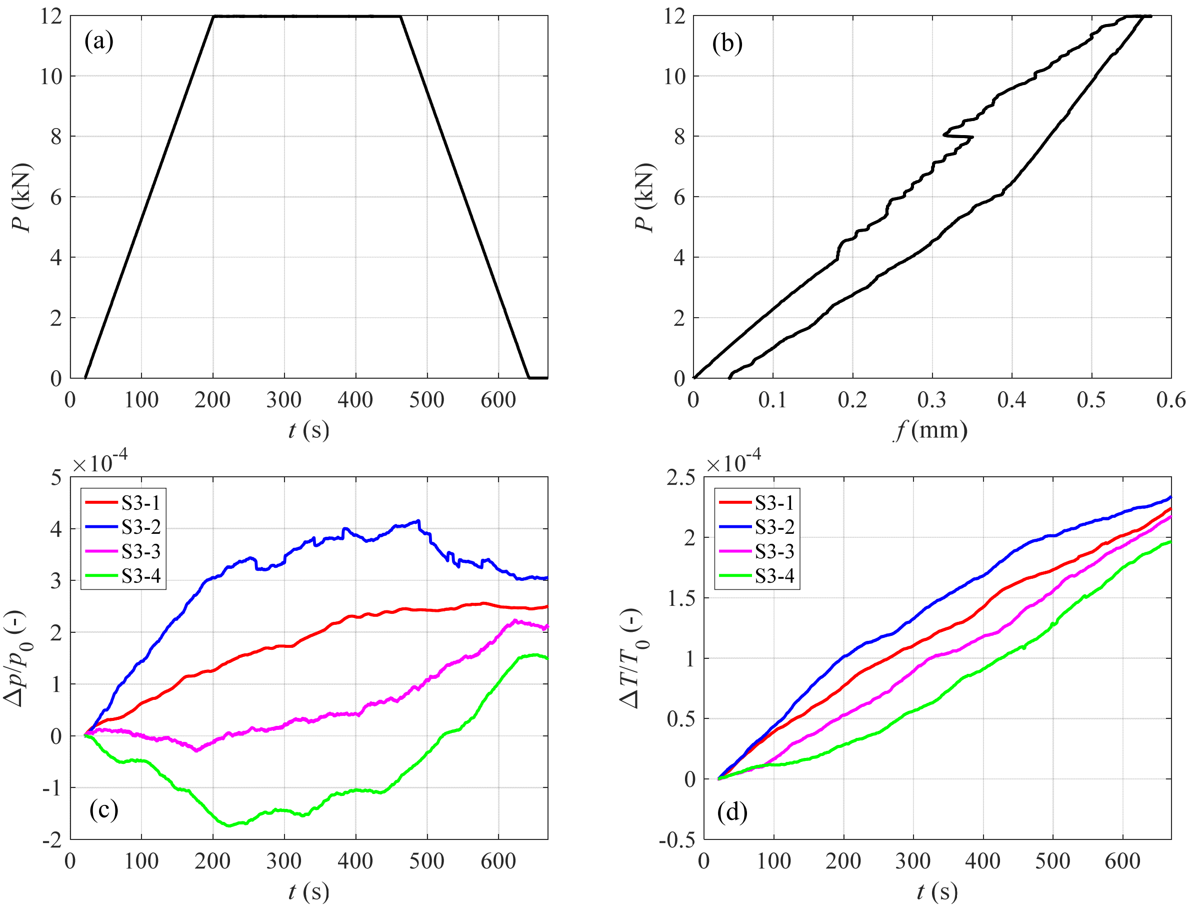

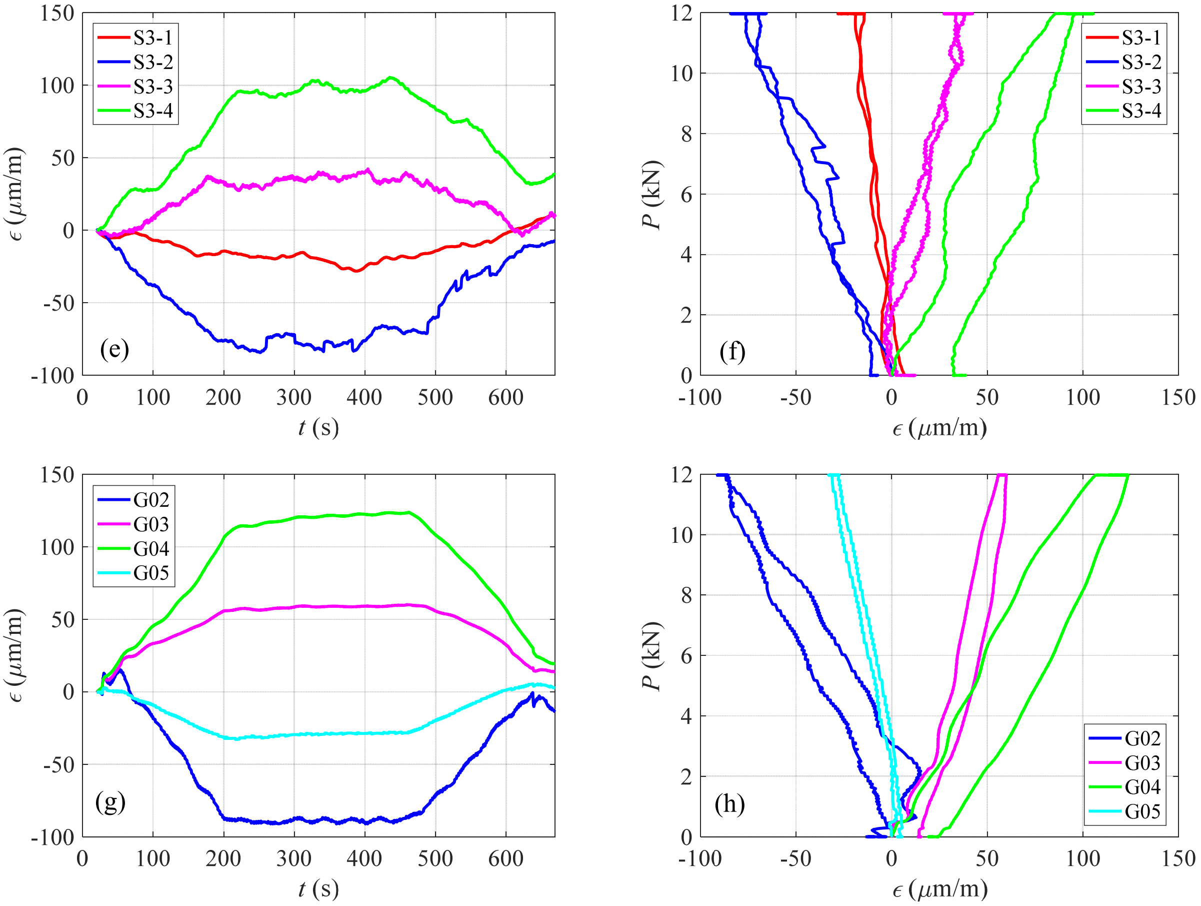

Fig. 5. Experimental measurements during load cycle #02: (a) applied load; (b) load-deflection curve; (c) pressure variations measured by the S3 sensors; (d) temperature variations measured by the S3 sensors; (e) strain reconstructed by the S3 sensors; (f) load-strain curves according to the S3 sensors; (g) strain measured by the G sensors (i.e. by conventional strain gauges); (h) load-strain curves according to the G sensors.

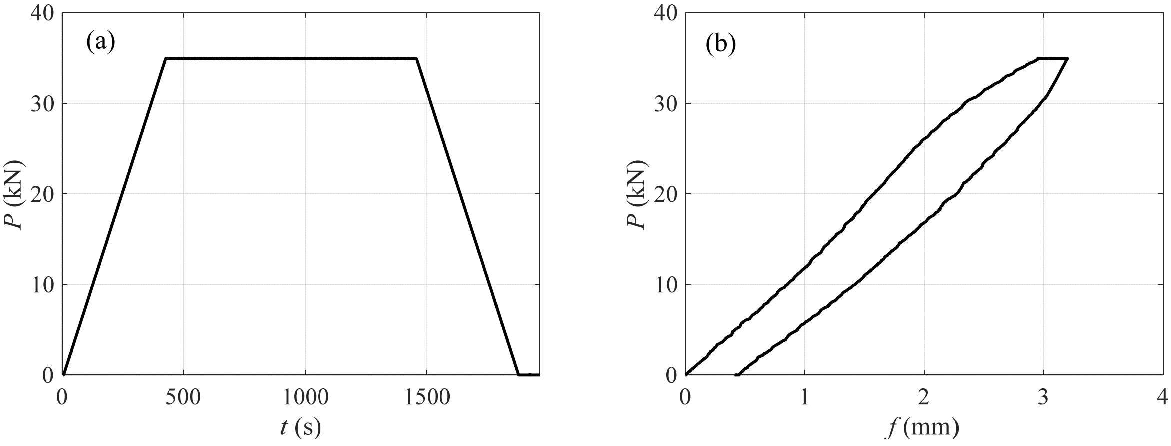

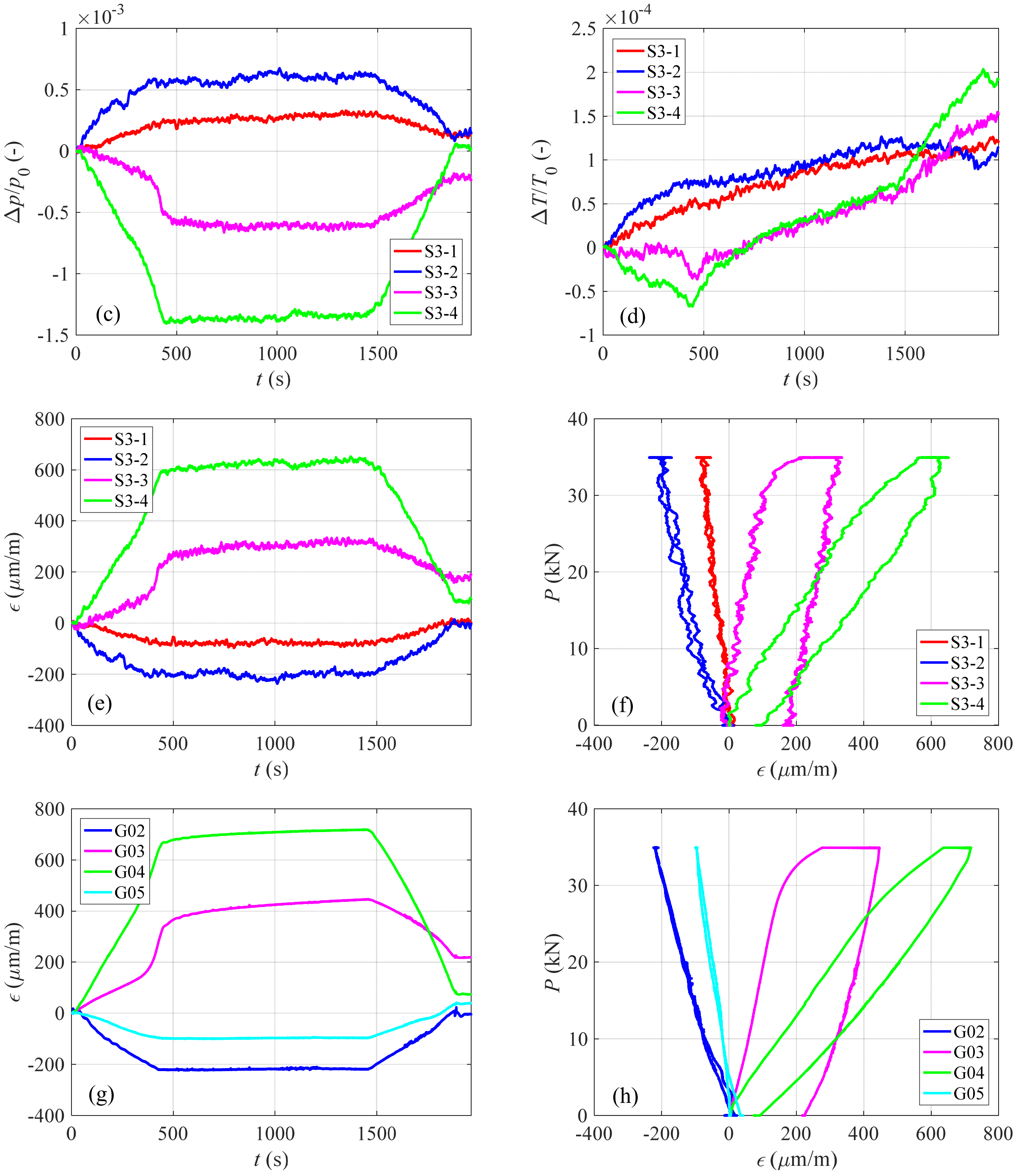

Fig. 6. Experimental measurements during load cycle #06: (a) applied load; (b) load-deflection curve; (c) pressure variations measured by the S3 sensors; (d) temperature variations measured by the S3 sensors; (e) strain reconstructed by the S3 sensors; (f) load-strain curves according to the S3 sensors; (g) strain measured by the G sensors; (h) load-strain curves according to the G sensors.

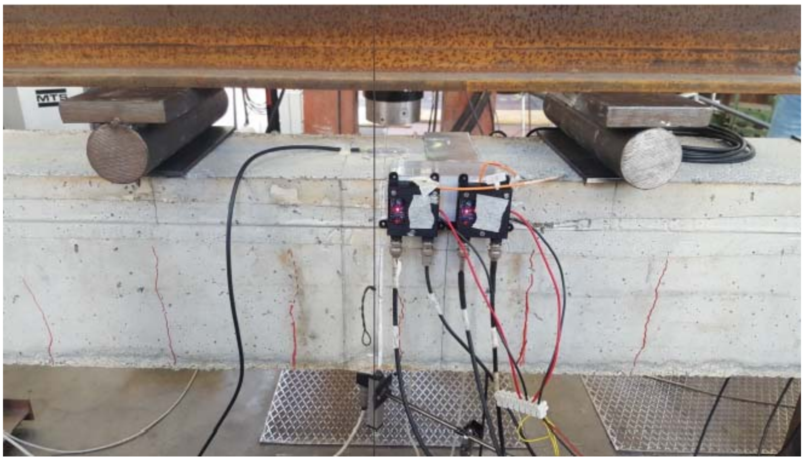

Fig. 7. Digital photo of the crack pattern at load cycle #06.

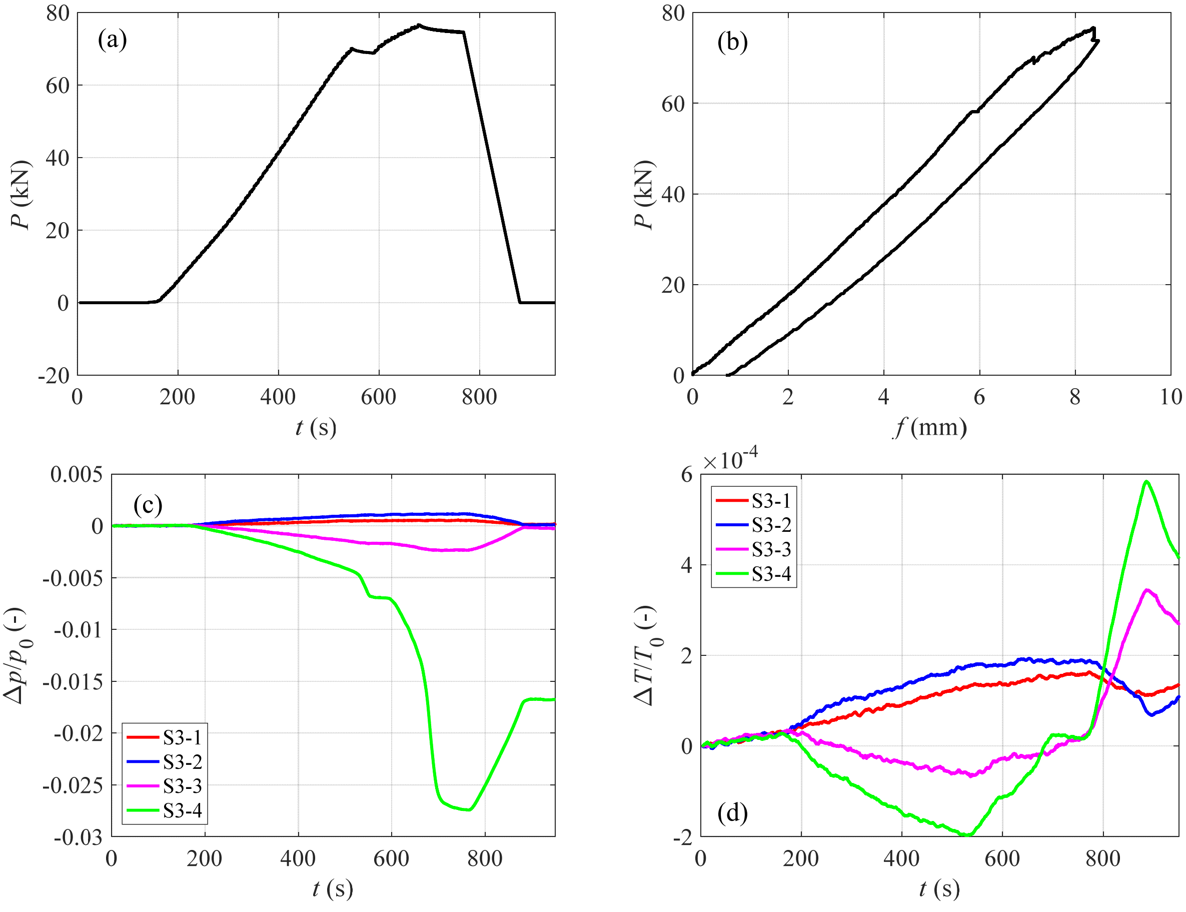

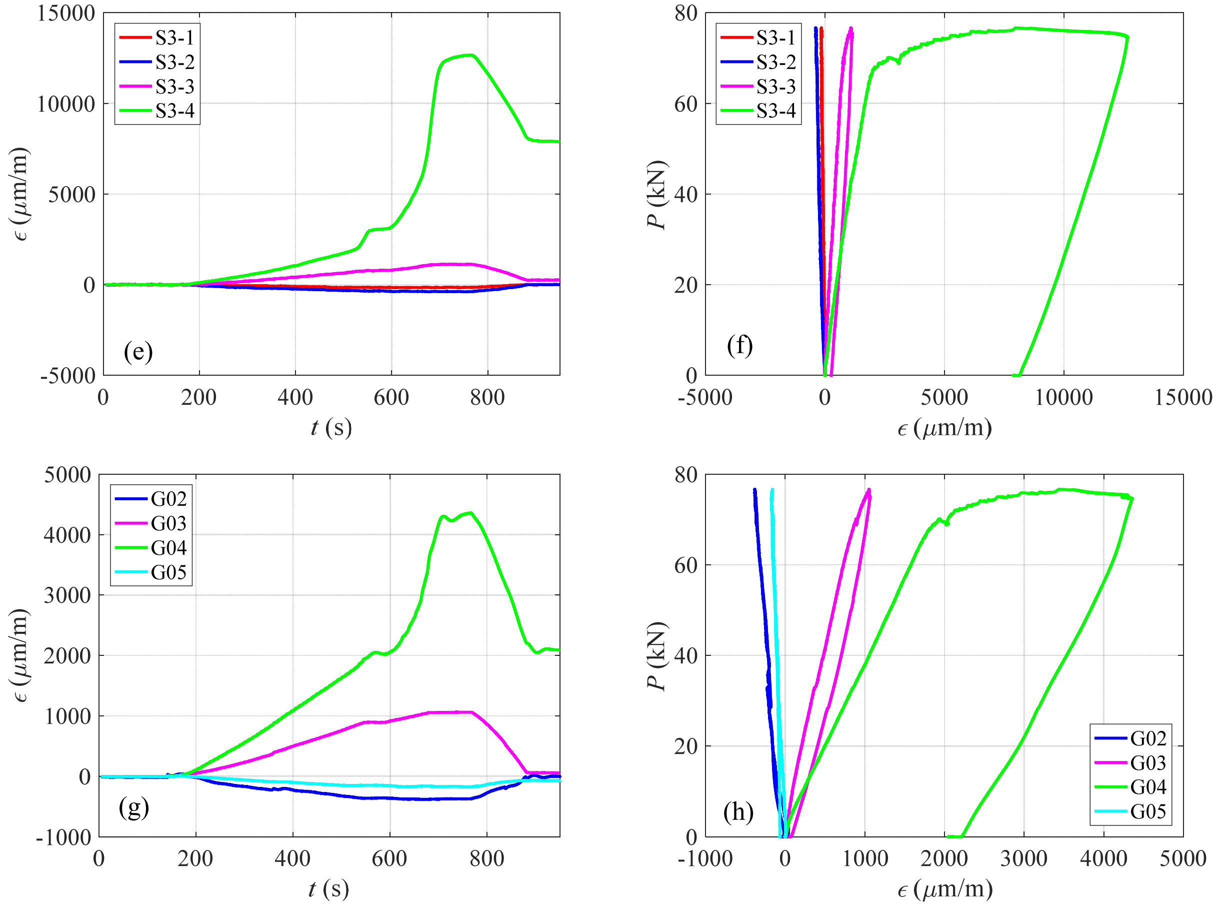

Fig. 8. Experimental measurements during load cycle #10: (a) applied load; (b) load-deflection curve; (c) pressure variations measured by the S3 sensors; (d) temperature variations measured by the S3 sensors; (e) strain reconstructed by the S3 sensors; (f) load-strain curves according to the S3 sensors; (g) strain measured by the G sensors; (h) load-strain curves according to the G sensors.

The results of the last load cycle test (#11) are presented in Figure 9. This is the load cycle, conducted under displacement control, which leads to the beam collapse. Figures 9a and 9b show the applied load time history and the beam load-deflection curve. The P-f relation appears nearly linear until P reaches the maximum value of the previous cycle (77 kN, around t = 425 s), then an approximately linear strain hardening branch begins, which leads to the ultimate load P_u = 88.2 kN and, after a short post-peak branch, to the sudden collapse of the instrumented bar, occurring at t = 770 s. This collapse instantaneously reduces the load bearing capacity of the beam to 24.3 kN, proportionally to the reduction of the total effective area of the transversal section of the steel bars in tension. The subsequent hardening branch testifies the residual strength capacity of the two 8 mm diameter bars in tension. The load is finally removed before reaching the collapse of these bars and therefore of the beam.

Observing the evolution of p and T in the S3 units (Figure 9c and 9d) and the corresponding estimations of ε (figure 9e to 9h), the following observations can be done:

- the S3-4 sensor opens (i.e. the cavity ceases to be hermetically closed, as it appears from the *p* time history in figure 9c) at t = 492 s (i.e. before the bar collapse), because of the large plastic strains accumulated around the hole. From this time on, although the S3-4 MEMS sensor still works, its strain estimations have no physical meaning (dashed lines in figures 9e and 9f). S3-4 opening is preceded by very large ε estimations (figure 9e), due to the large inelastic behaviour of the steel material around the cavity (Figure 9f). This is particularly evident after t = 425 s (figure 9e), when ε corresponds to the maximum value reached in the previous load cycle. After t = 400 s, the energy dissipation produced by the large plastic deformations around the cavity is also responsible for a rapid temperature increase (Figure 9d), which will continue even after the sensor opening and until the bar collapse (t = 770 s).
- The other three S3 units are effective and work all through the test. Before the bar collapse, S3-3 has already experienced local plastic deformations, particularly after t = 425 s (strain level of the previous load cycle), while S3-1 and S3-2 are still in the elastic range. Interestingly, after t = 420 s, the S3-2 sensor, initially compressed, experiences a progressive strain increase (in sign) until finally working in tension. This occurs because, as cracking in the beam midsection increases, the neutral axis progressively rises and eventually exceeds the position of the top bar where the S3-2 sensor is embedded. At collapse (t = 770 s), S3-3 and S3-1 sense the stress drop due to the sudden load reduction, while S3 increases its tension as the neutral axis further rises.

The same qualitative trends can be recognized in the strain measurements provided by the G sensors (figures 9i and 9j). In quantitative terms, as already observed when commenting the previous load cycle, the G strains tend to appear smaller than the S3-2 strains when large local plastic deformations occur. This, however, seems not to be the case for the co-located pair S3-2/G02, arguably due to its particular load reversal time history. Significantly, two of the four G sensors fail during loading (dashed lines in figures 9i and 9j): G04 fails at t = 425 s, even before the failure of the co-located S3-4 sensor; and G03 fails at the bar collapse (t = 770 s). It can be concluded that, of the six strain gauges initially installed on the steel bars, only two are still working at the end of the experimental campaign.

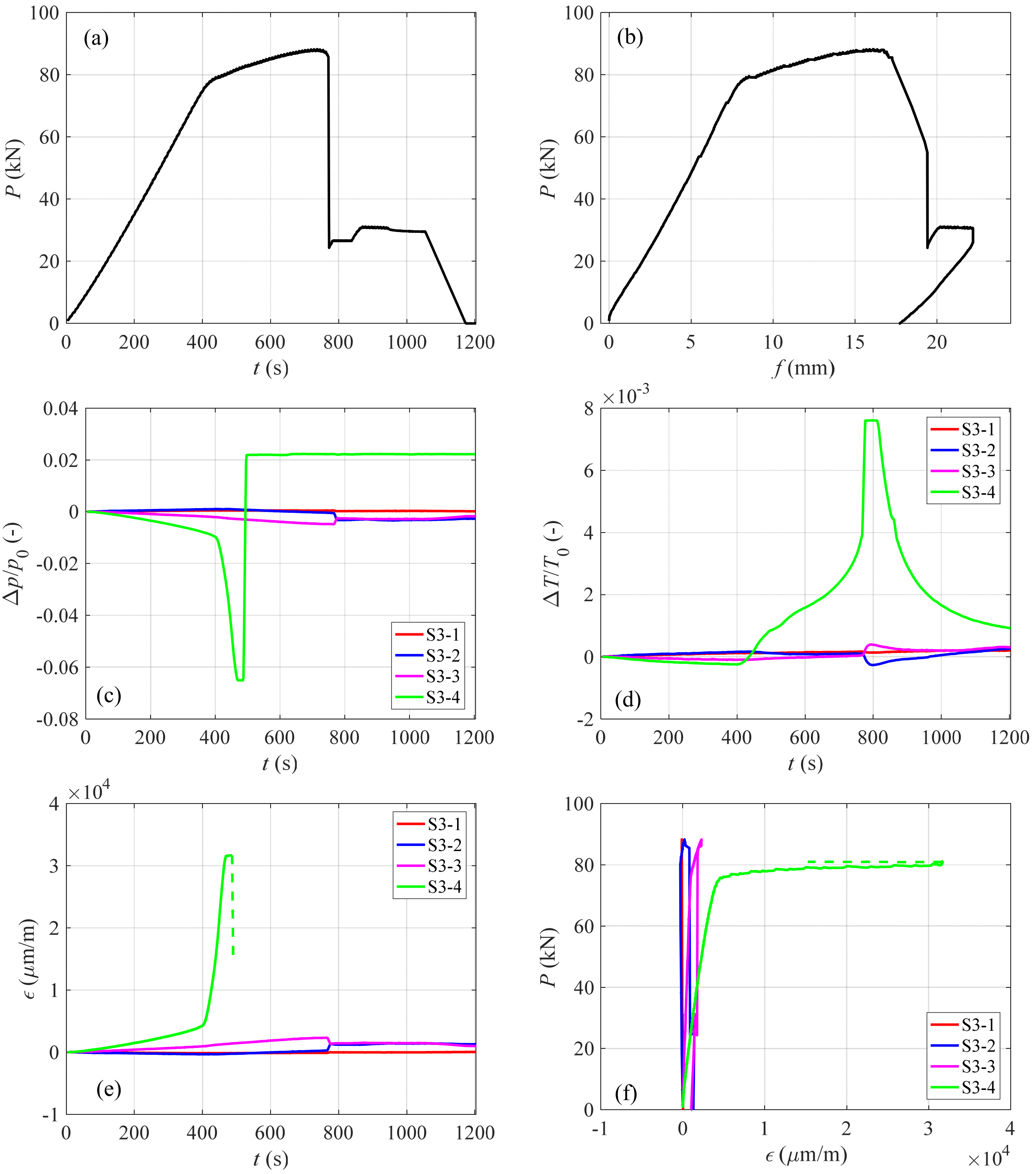
(a)
P (kN)
t (s)
(b)
P (kN)
f (mm)
(c)
$\Delta p/p_0$ (-)
t (s)
S3-1
S3-2
S3-3
S3-4
(d)
$\times 10^{-3}$
$\Delta T/T_0$ (-)
t (s)
(e)
$\times 10^4$
ϵ (μm/m)
t (s)
(f)
P (kN)
ϵ (μm/m)
$\times 10^4$

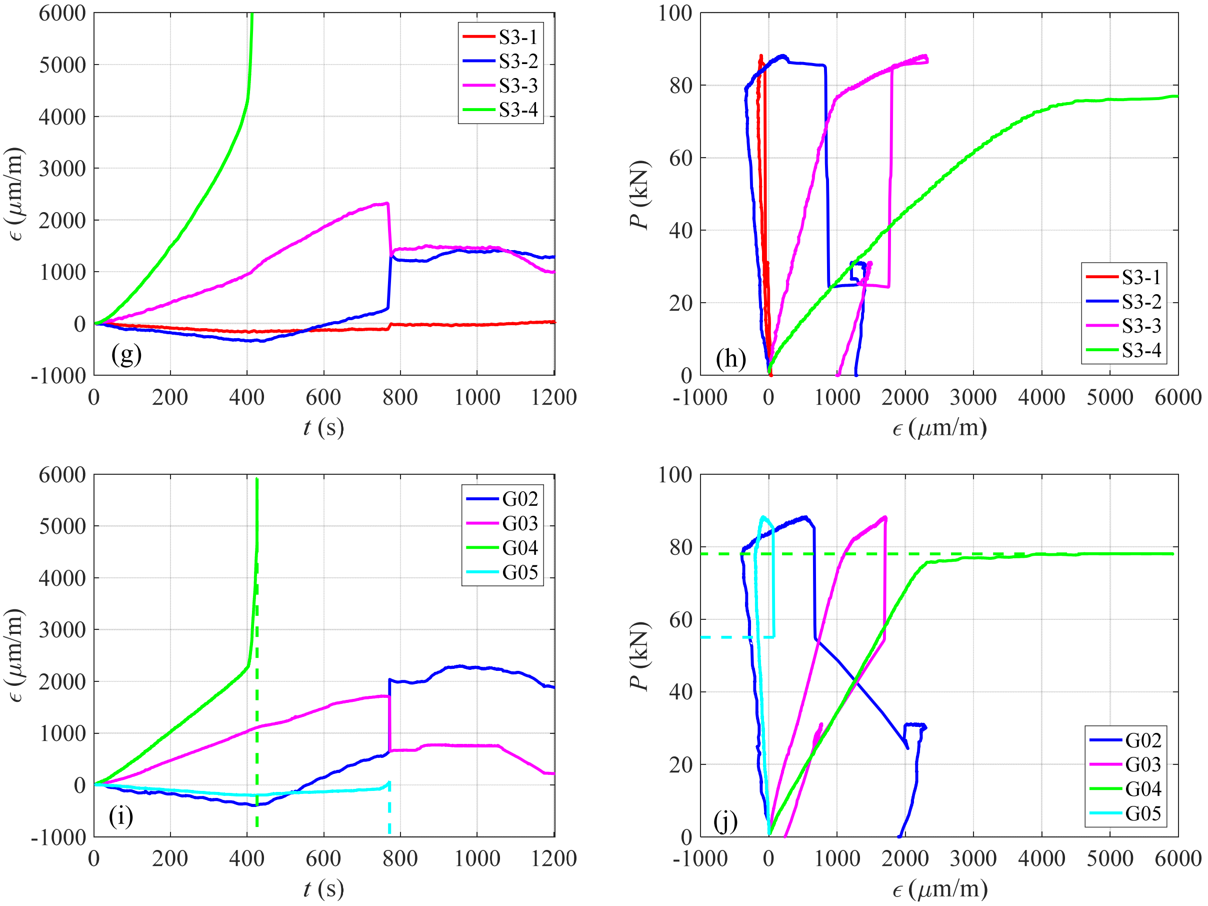

Fig. 9. Experimental measurements during load cycle #11: (a) applied load; (b) load-deflection curve; (c) pressure variations measured by the S3 sensors; (d) temperature variations measured by the S3 sensors; (e) strain reconstructed by the S3 sensors (full view); (f) load-strain curves according to the S3 sensors (full view); (g) strain reconstructed by the S3 sensors (zoomed view); (h) load-strain curves according to the S3 sensors (zoomed view); (i) strain measured by the G sensors; (j) load-strain curves according to the G sensors.

To provide a comprehensive view of the entire experimental campaign, the cumulative effects of all load cycles are summarized in Figures 10 and 11, respectively in terms of load-deflection and load-strain curves. Each new cycle starts from the residuals accumulated in the previous cycles. The load-strain curves are plotted until the instant of application of the ultimate load P_u, except for the S3-4/G04 pair, where they are both terminated at the instant of G04 failure.

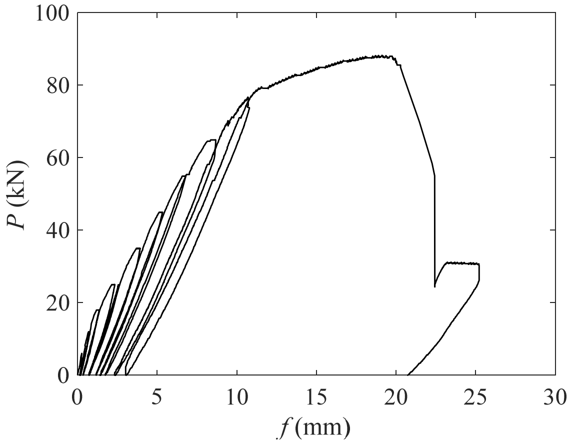

Fig. 10. Cumulative beam load-deflection curve under repeated load cycles.

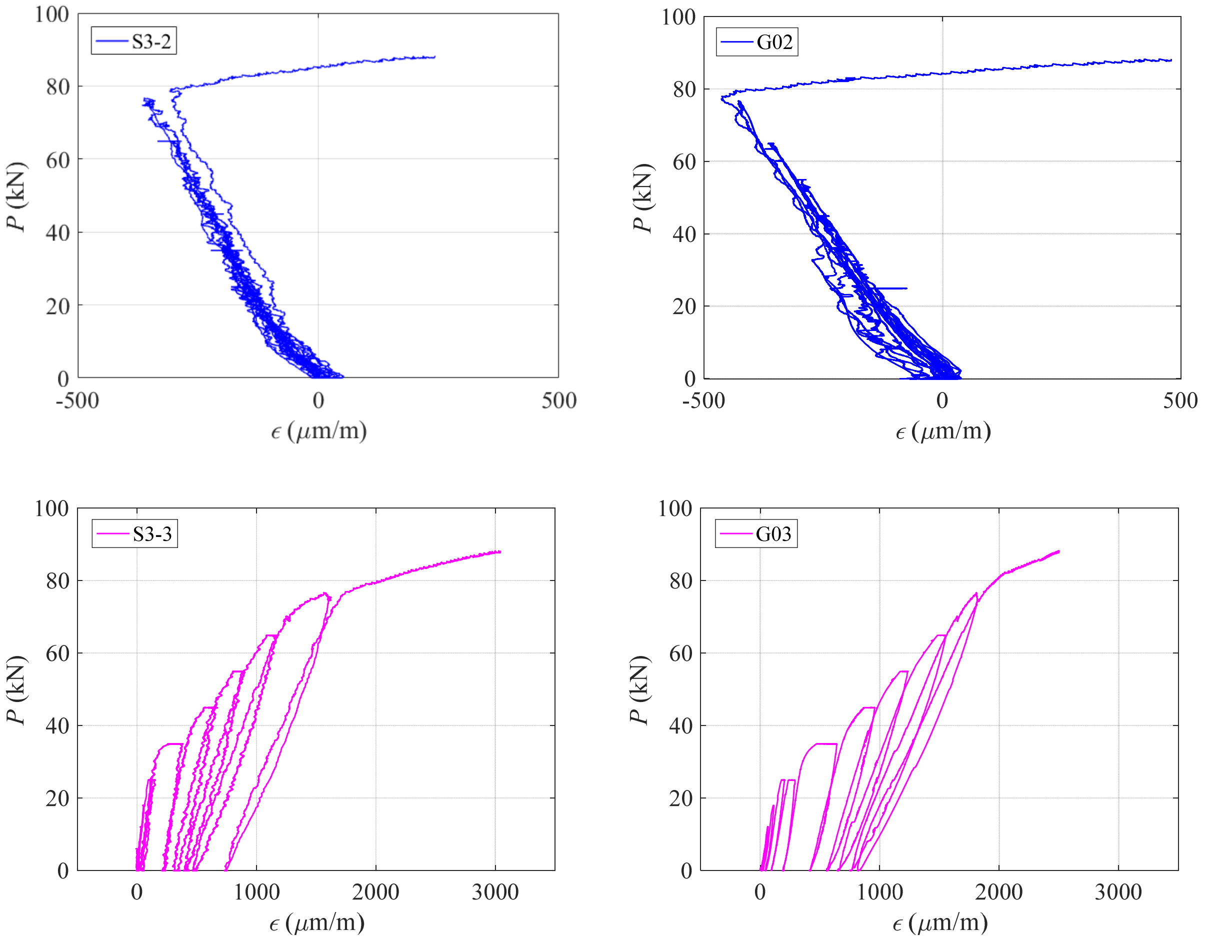

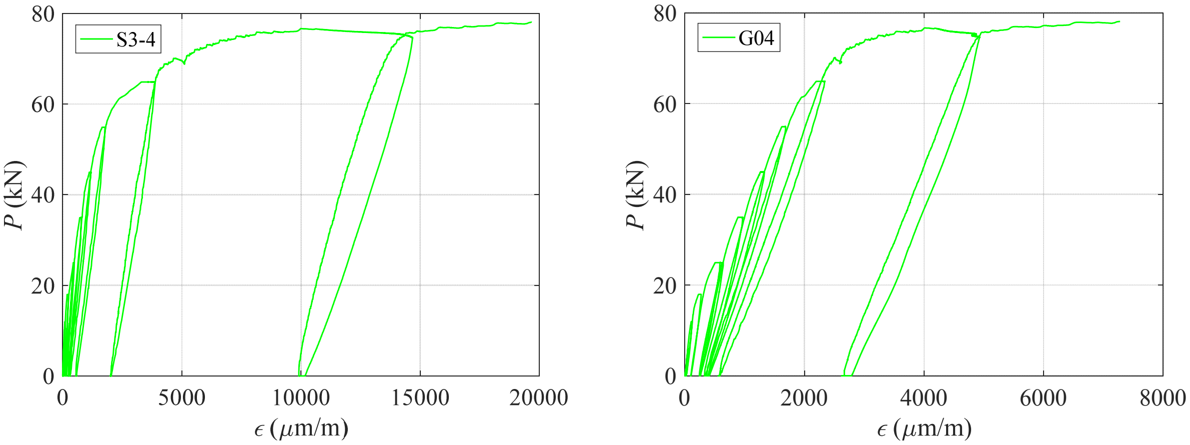

Fig. 11. Cumulative load-strain curves under repeated load cycles, for the three pairs of co-located S3 and G sensors.

By observing the loading phase of each load cycle (also see again Table 2), a satisfactory correlation between the strain measures provided by the S3 and the G sensor types can be appreciated. For the two co-located pairs of sensors measuring positive strains (tension), the S3 to G strain ratio appears an increasing function of *P*, because of the lesser sensibility of the strain gauges to cavity volume variations as plastic deformations occur around the cavity. For the only co-located pair of sensors measuring negative strains (compression), the ratio is more stable and close to 1, except for the last cycle, where the rising of the neutral axis induces the strain sign reversal. This difference between tensed and compressed sensors is likely due to the smaller strain range experienced by the compressed sensors, which keeps elastic the bar around the cavity. To show the relation existing between the cavity volume variations (measured by the S3 units) and the local bar axial deformations around the cavity (measured by the strain gauges), Figure 12 compares the strain measurements provided by, respectively, S3-4 and G04 at load cycle #10. The red dotted line in Figure 12a represents the ideal case of a unit S3 to G strain ratio, whereas the red dotted line in Figure 12b represents the 10% value of the relative error (in absolute value) between the two measures. Excluding strain values lower than 100 μm/m, highly affected by measurement noise, a substantial equivalence between the S3 and the G measures is appreciable for strain values up to 1250 μm/m, in agreement with the tests reported in [28]. The error exceeds 10% when the strain exceeds 1750 μm/m, i.e. when the applied load *P* exceeds 71% of the ultimate load P_u. In the 100÷1750 μm/m range, the average error is 4.7%. Out of this range, the S3 to G strain ratio results an increasing function of *P*, as already observed for all co-located pairs of sensors measuring positive strains.

A satisfactory correlation between S3 and G measurements can be recognized also by looking at the cumulative effects produced by repeated load cycles (Figure 11). A certain difference is observed at small loads, where the G sensors appear to detect larger plastic strains during the phases of constant loading. This difference may be partly the effect of the beam cracking and the consequent slip between steel and concrete, possibly affecting strain gauges measures.

In general, both S3 and G sensors perform acceptably during all load cycles, except when the loading level is very close to collapse. S3 units prove more robust than G sensors, since three S3 units out of the four installed survive the tests, whereas only two G sensors of the six initially installed avoid failure.

The load-deflection curve in Figure 10 reveals the limited ductility of the beam. The cumulative deflection at the maximum load, equal to 20 mm, is only slightly larger than the cumulative deflection at the beginning of the hardening branch, approximately equal to 11 mm. This limited ductility is due to the scarce ductility of the instrumented bar and to the limited relative contribution to the overall bending capacity given by the ordinary bars, which provide a limited sectional area. This indicates that a significant effort shall be devoted in future studies to locally increase the strength and ductility of the instrumented bar around the cavity through the realization of an appropriate additional rib. It also suggests that, in the absence of such solution, the S3 system should be used only in cases when no significant ductility is required, or in cases where the percentage contribution of the instrumented bar to the overall sectional capacity is small (e.g. large r.c. sections with several ordinary bars).

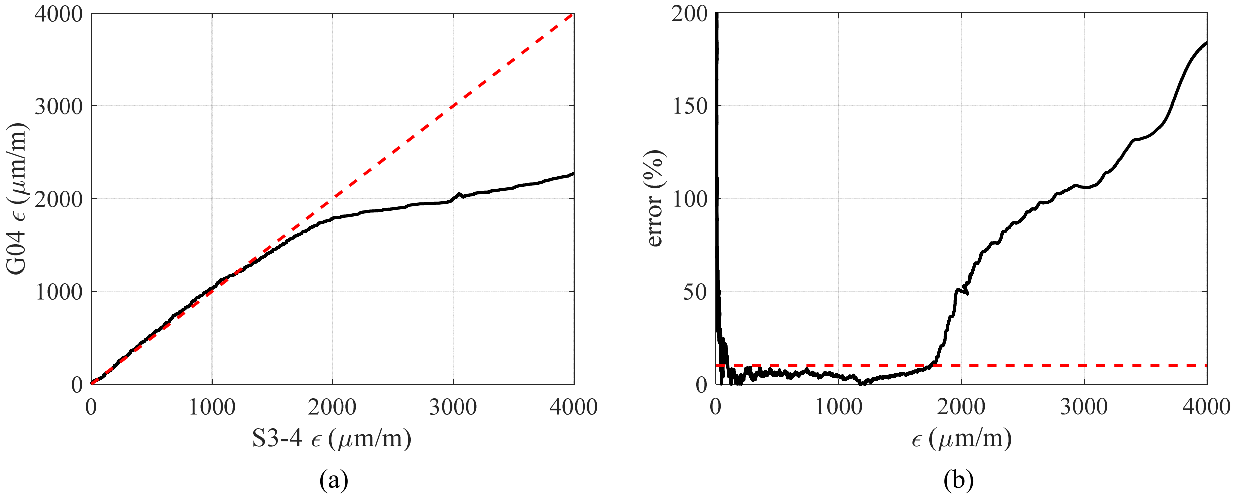

(a) (b)

Fig. 12. Comparison between the strain measurements provided by S3-4 and G04 at load cycle #10. The dotted red lines represent: in (a) the ideal case of a unit S3 to G strain ratio; in (b) the 10% relative discrepancy between the two measures.

5 Conclusions

The present paper reports the results of an experimental campaign aimed at testing the performance of a new strain monitoring system, called S3, installed in a reinforced concrete beam subjected to repeated loading-unloading cycles of increasing amplitude until collapse. In its basic configuration, the S3 system consists of a reinforcing steel bar hosting one or more sealed cavities (sensing units), each containing a barometric pressure sensor able to read pressure and temperature of the cavity, and therefore to deduce the bar local deformation. In the proposed experiment, two instrumented bars are incorporated in the reinforcing cage of the tested beam, each bar being equipped with two S3 units as well as with some conventional electrical strain gauges glued on the bar surface, partly co-located in the same position as the S3 units, partly at a certain distance. Electrical strain gauges are here used as a baseline reference for evaluating the sensing performance of the new S3 units, but also to test the robustness of conventional transducers when installed in reinforced concrete structures.

The experimental campaign generally reveals a satisfactory agreement between the strain measures provided by, respectively, the S3 units and the strain gauges, for a large range of load levels. At low load levels ($\varepsilon < 100$ μm/m), the S3 measures appear noisier, but their underlying trends still match well with the strain gauges readings. Both sensor types reveal cyclic hysteresis in the load-strain curves, probably due to micro-cracking. At medium load levels (up to $\varepsilon < 1750$ μm/m), when the instrumented bars still respond in their linear elastic range, a good agreement is observed between S3 and strain gauges readings, while the noise in S3 measures becomes nearly negligible. Significant hysteresis is observed in the load-strain curves of both sensor types, particularly for sensors located close to the activation of new cracks. At higher load levels ($\varepsilon > 1750$ μm/m), corresponding to the insurgence of large plastic deformations around the S3 cavities, the strains measured by the S3 units become increasingly larger than the strains measured by the co-located strain gauges, because plastic deformations affect more the cavity volume variations then the average axial strains at the bar surface around the cavity.

On the other hand, the S3 system shows a good robustness in all the phases of the test campaign, from concrete casting to collapse, whereas several of the installed strain gauges undergo failure, either during casting or during loading. This increased robustness and durability, due to the S3 sensing units being embedded in a mechanically and chemically protected environment, is indeed one of the main advantages of the S3 system, with respect to existing arrangements of strain sensors adhered to the bar surface, instead prone to impacts, abrasion, and stress concentrations at the steel-concrete interface. In the face of this fundamental advantage of S3, and of its acceptable sensibility with respect to conventional strain gauges, the relative complexity of the manufacturing process is believed to be admissible in many real applications, also considering that drastic simplifications and cost reductions will come from the standardization and industrialization of the production process, currently under study.

From a structural perspective, the presence of the cavity reduces both the strength and the ductility of the bar, and then of the whole structural element where that bar is incorporated. Further developments are under study to locally modify the geometry of the bar around the cavity so as to completely restore its original mechanical properties. Expectedly, these modifications will also extend the measuring range where a linear correlation exists between cavity volume variations and bar axial deformations. Yet, despite still being in an early stage of development, the tested S3 system already proves a promising solution. Its low cost and robustness as well as its thermal self-compensation features make it a good candidate for future real field monitoring applications.

References

[1] Lynch, JP & Loh, KJ (2006) A summary review of wireless sensors and sensor networks for structural health monitoring, Shock Vib. Digest, vol. 38, no. 2, 91-128.
[2] Spencer, BF Jr., Park, J-W, Mechitov, KA, Jo, H, Agha, G (2017) Next generation wireless smart sensors toward sustainable civil infrastructure, Procedia Engineering, vol. 171, 5-13.
[3] Pentaris FP, Stonham J, Makris JP (2014), A cost effective wireless structural health monitoring network for buildings in earthquake zones, Smart Mater. Struct. 23, 105010.
[4] Maruccio C, Quaranta G, De Lorenzis L, Monti G (2016) Energy harvesting from electrospun piezoelectric nanofibers for structural health monitoring of a cable-stayed bridge, Smart Mater. Struct. 25, 085040.
[5] Ceravolo R., Matta E., Quattrone A., Zanotti Fragonara L. (2017) Amplitude dependence of equivalent modal parameters in monitored buildings during earthquake swarms, arthquake Engng Struct. Dyn. 46, 2399-2417.
[6] Collins J, Mullins G, Lewis C, Winters D (2014) State of the Practice and Art of Structural Health Monitoring of Bridge Substructures, FHWA-HRT-09-040.
[7] Mutlib, NK, Baharom, SB, El-Shafie, A, Nuawi, MZ (2016) Ultrasonic health monitoring in structural engineering: Buildings and bridges, Structural Control and Health Monitoring 23(3), 409-422.
[8] Ge, Y, Elshafie MEB, Dirar, S, Middleton, CR, The response of embedded strain sensors in concrete beams subjected to thermal loading, Construction and Building materials 70, 279-290.
[9] Montanini, R, Recupero, A, De Domenico, F, Freni, F (2016) Strain sharing assessment in woven fiber reinforced concrete beams using fiber Bragg grating sensors, Sensors (Switzerland) 16(10).
[10] Netti A, Fiore A, Monaco P, Marano GC (2015) Investigation of traffic-induced vibrations on a historic swing bridge in Italy, International Journal of Mechanics 9, 53-60.
[11] Fiore A, Marano GC (2018), Serviceability Performance Analysis of Concrete Box Girder Bridges Under Traffic-Induced Vibrations by Structural Health Monitoring: A Case Study, International Journal of Civil Engineering 16(5), 553-565.
[12] Gagar, D, Foote P, Irving P (2014) A novel closure based approach for fatigue crack length estimation using the acoustic emission technique in structural health monitoring applications, Smart Mater. Struct. 23, 105033.
[13] Hester, D, Brownjohn, J, Bocian, M & Xu, Y (2017) Low cost bridge load test: Calculating bridge displacement from acceleration for load assessment calculations, Engineering Structures 143(7), 358-374.
[14] Gomez, JA, Ozdagli, AI, Moreu, F (2017) Reference-free dynamic displacements of railroad bridges using low-cost sensors. J. Intell. Mater. Syst. Struct. 1-15.
[15] Hester D., Brownjohn J., Bocian M., Xu Y., Quattrone A. (2018) Using inertial measurement units originally developed for biomechanics for modal testing of civil engineering structures, Mechanical Systems and Signal Processing 104, 776-798.
[16] Hu Liu, Yilong Li, Kun Dai, Guoqiang Zheng, Chuntai Liu, Changyu Shen, Xingru Yan, Jiang Guo, Zhanhu Guo (2016) Electrically conductive thermoplastic elastomer nanocomposites at ultralow graphene loading levels for strain sensor applications, Journal of Materials Chemistry C 4, 157-166.
[17] Chao Hu, Zeyu Li, Yalong Wang, Jiachen Gao, Kun Dai, Guoqiang Zheng, Chuntai Liu, Changyu Shen, Haixiang Song, Zhanhu Guo (2017) Comparative assessment of the strain-sensing behaviors of polylactic acid nanocomposites: reduced graphene oxide or carbon nanotubes, J. Mater. Chem. C 5, 2318-2328.
[18] Hu Liu, Qianming Li, Shuaidi Zhang, Rui Yin, Xianhu Liu, Yuxin He, Kun Dai, Chongxin Shan, Jiang Guo, Chuntai Liu, Changyu Shen, Xiaojing Wang, Ning Wang, Zicheng Wang, Renbo Wei, Zhanhu Guo (2018) Electrically conductive polymer composites for smart flexible strain sensors: a critical review, Journal of Materials Chemistry C 6, 12121-12141.
[19] Yang Lu, Manik Chandra Biswas, Zhanhu Guo, Ju-Won Jeon, Evan K. Wujcik (2019) Recent developments in bio-monitoring via advanced polymer nanocomposite-based wearable strain sensors, Biosensors and Bioelectronics 123, 167-177.

[20] Laflamme S, Kollosche M, Connor JJ, and Kofod G. (2012) Robust flexible capacitive surface sensor for structural health monitoring applications Journal of Engineering Mechanics 139, 879-85.

[21] Bay BK, Smith TS, Fyhrie DP, Saad M (1999) Digital Volume Correlation: Three-dimensional Strain Mapping Using X-ray Tomography. Exp Mech 39, 217–26.

[22] Bouterf A, Roux S, Hild F, Adrien J, Maire E, Meille S (2014) Digital volume correlation applied to x-ray tomography images from spherical indentation tests on lightweight gypsum. Strain 50(5), 444–453]

[23] Prieto, M, Tanner, P, Andrade, C, Fernandex, M 2013 Experimental and numerical study of bond response in structural concrete with corroded steel bars, IABSE Workshop on Assessment, Upgrading and Refurbishment of Infrastructures; Rotterdam, Netherlands, 1752-1759.

[24] Barrias, A, Casas, JR, Villalba, S 2016, A review of distributed optical fiber sensors for civil engineering applications, *Sensors* 16(748), 1-35.

[25] Mains, RM (1951) Measurement of the distribution of tensile and bond stresses along reinforcing bars, ACI Journal 48(11), 225-252.

[26] Lagier, L, Massicotte, B, Charron JP (2016) Experimental investigation of bond stress distribution and bond strength in unconfined UHPFRC lap splices under direct tension, Cement and Concrete Research 74, 26-38.

[27] Tondolo, F (2016) An integrated system and method for measuring deformations and/or stresses in one-dimensional elements, *Patent* n° 102016000118077, Italy. PC1558CF, European Patent Office.

[28] Tondolo F, Cesetti A, Matta E, Quattrone A, Sabia D (2018) Smart reinforcement steel bars with lowcost MEMS sensors for the structural health monitoring of RC structures, Construction and Building Materials 173, 740-753.